The Vanishing Confinement Regime in THz HgTe Nanocrystals Studied Under Extreme Conditions of Temperature and Pressure

Stefano Pierini, Francesco Capitani, Michael Scimeca, Sergei Kozlov, Debora Pierucci, Rodolphe Alchaar, Claire Abadie, Adrien Khalili, Mariarosa Cavallo, Tung Huu Dang, et al.

To cite this version:

Stefano Pierini, Francesco Capitani, Michael Scimeca, Sergei Kozlov, Debora Pierucci, et al.. The Vanishing Confinement Regime in THz HgTe Nanocrystals Studied Under Extreme Conditions of Temperature and Pressure. Journal of Physical Chemistry Letters, 2022, pp.6919-6926. 10.1021/acs.jpclett.2c01636 . hal-03737454

HAL Id: hal-03737454
https://hal.science/hal-03737454

Submitted on 25 Jul 2022

The Vanishing Confinement Regime in THz HgTe Nanocrystals Studied Under Extreme Conditions of Temperature and Pressure

Stefano Pierini[1,2], Francesco Capitani[3], Michael Scimeca[4], Sergei Kozlov[5], Debora Pierucci[2], Rodolphe Alchaar[1], Claire Abadie[1], Adrien Khalili[1], Mariarosa Cavallo[1], Tung Huu Dang[1], Huichen Zhang[1], Erwan Bossavit[1], Charlie Gréboval[1], José Avila[3], Benoit Baptiste[6], Stefan Klotz[6], Ayaskanta Sahu[4], Cheryl Feuillet-Palma[5], Xiang Zhen Xu[5], Abdelkarim Ouerghi[2], Sandrine Ithurria[5], James K. Utterback[1], Sebastien Sauvage[2], Emmanuel Lhuillier[1*]

[1] Sorbonne Université, CNRS, Institut des NanoSciences de Paris, INSP, F-75005 Paris, France.
[2]Université Paris-Saclay, CNRS, Centre de Nanosciences et de Nanotechnologies, CNRS, 10 Boulevard Thomas Gobert, 91120 Palaiseau, France

[3]Synchrotron-SOLEIL, Saint-Aubin, BP48, F91192 Gif sur Yvette Cedex, France.
[4]Department of Chemical and Biomolecular Engineering, New York University, Brooklyn, NY 11201, USA
[5] Laboratoire de Physique et d'Etude des Matériaux, ESPCI-Paris, PSL Research University, Sorbonne Université Univ Paris 06, CNRS UMR 8213, 10 rue Vauquelin 75005 Paris, France.
[6]Sorbonne Université, CNRS, Institut de Minéralogie, de Physique des Matériaux et de Cosmochimie, IMPMC, F-75005 Paris, France.

Abstract: While HgTe nanocrystals (NCs) in the mid infrared have reached a high maturity, their far infrared counter-parts remain far less studied, raising the need for an in-depth investigation of the material before efficient device integration can be considered. Here, we explore the effect of temperature and pressure on the structural, spectroscopic and transport properties of HgTe NCs displaying an intraband absorption at 10 THz. The temperature leads to a very weak modulation of the spectrum as opposed to what was observed for strongly confined HgTe NCs. HgTe NC films present ambipolar conduction with a clear prevalence of electron conduction as confirmed from transistor and thermoelectric measurements. Under pressure application, the material undergoes phase transitions from the zinc blende to cinnabar and later to rock salt that we reveal using joint X-ray diffraction and infrared spectroscopic measurements. We discuss how the pressure existence domain of each phase is affected by the particle size.

TOC graphic

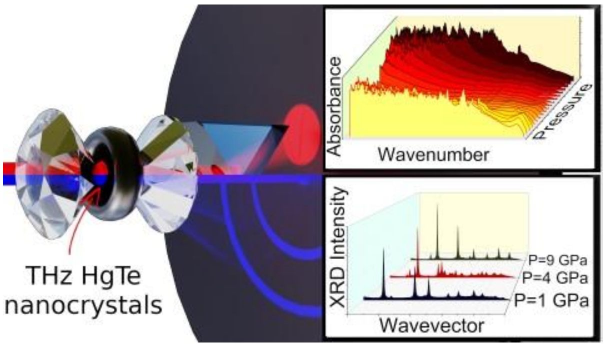

Keywords: HgTe, nanocrystals, pressure, electronic structure, phase transition, terahertz.

*To whom correspondence should be sent: el@insp.upmc.fr

HgTe nanocrystals[1,2] (NCs) have reached a high maturity that enables the demonstration of complex devices such as lasers[3], LEDs[4–6], IR sensors with carrier density[7–10] and light–matter control[11–14] as well as cameras[15–17]. All of these results have been obtained with NCs that absorb in the near to mid wave infrared. Thanks to the semimetal nature of HgTe, the absorption spectrum of NCs can be tuned up to the THz frequency range, which corresponds to a spectral range where the NC properties remain underexplored[18]. Goubet *et al* reported a strategy to grow large HgTe NCs[19] with sizes larger than the Bohr radius[20] (40 nm), which is large compared to other II-VI semiconductors due to the high dielectric constant and low effective electron mass of HgTe. They demonstrated that, in the THz range, absorption occurs through an intraband transition[15,21–25] whose maximum can be brought up to 60 µm (20 meV, 166 cm^{-1} or 5 THz). Later, Apretna *et al* investigated the carrier dynamics in such THz absorbing HgTe NCs[26]. They found that intraband relaxation occurs within a few ps and with a decay rate of 0.5 eV.ps^{-1}, which is close to the values observed in more strongly confined HgTe NCs with sparser densities of states[4,27].

The THz HgTe NCs offer an interesting playground to probe an electronic state between the bulk and the strongly confined regimes[28]. Here, we explore how temperature and pressure affect the structural and electronic properties of an HgTe NCs assembly in this intermediate regime where confinement is almost vanished.

The phase diagram of HgTe as a function of pressure and temperature has been extensively investigated for the bulk[29–31] and thin film[32] form. The material is known to experience a series of structural phase change as pressure is applied. The zinc blende phase, stable under room pressure, is a semimetal phase, which transforms into a semiconductor when confinement is introduced. Under higher pressure the material turns[29–31] to cinnabar and then to the rock salt phase which are respectively a semiconductor and a metallic phase. Here, we show that the intraband feature in the THz appears quite stable all over the explored temperature range and discuss how the structural phases of HgTe have their domain of existence affected by the finite particle size.

We start by growing large HgTe NCs presenting intraband absorption at ≈300 cm^{-1} or 10 THz (see **Figure 1**b). Above 800 cm^{-1}, we observe a rise of the absorption that can be attributed to interband absorption. The Raman spectrum (see the inset **Figure 1**b) displays two main features associated with optical phonons that are respectively the TO phonon at 120 cm^{-1} and LO phonon at 141 cm^{-1}. Thus, we can confidently attribute the remaining narrow peaks (from 700 to 1000 cm^{-1}, see Figure S2 and 3) observed in the infrared spectrum to organic bonds coming from ligands. Electronic microscopy (**Figure 1**a and S1) shows particles around 15 nm in size, which is also confirmed as the Scherrer length obtained by fitting the linewidth of the X-ray diffraction pattern, see Figure S5.

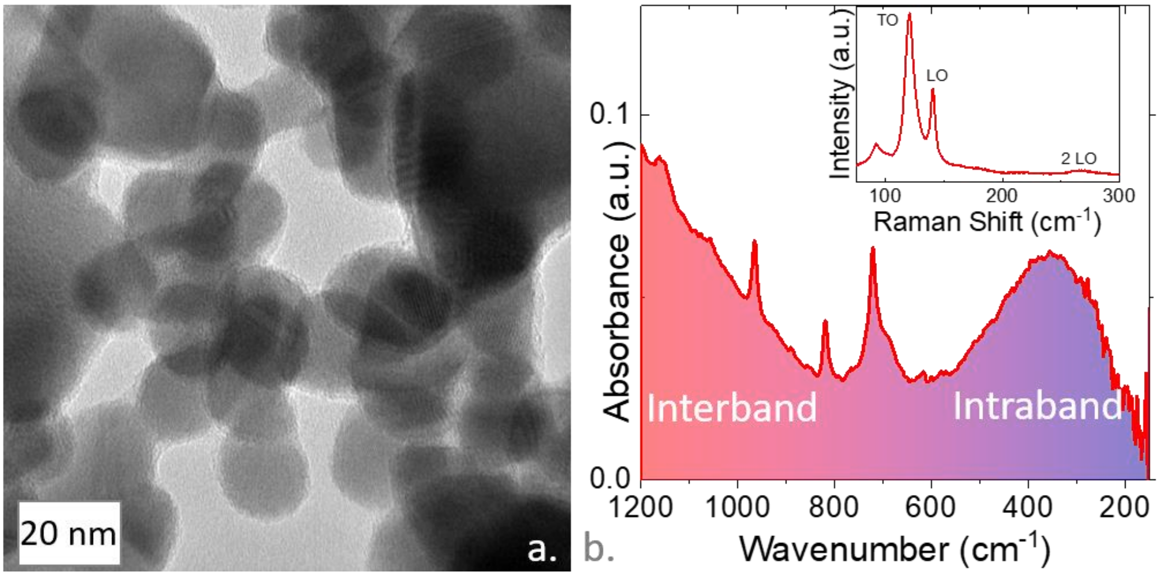

Figure 1 Structural and spectroscopic properties of THz HgTe NCs. *a. TEM image of THz HgTe NCs. b. Infrared spectrum of THz HgTe NCs. Inset: Raman spectrum of THz HgTe NCs.*

We then explore the effect of temperature on the spectral and transport properties of these HgTe NCs, see **Figure 2**. In the 300 K to 60 K range, the infrared absorption spectrum displays very limited changes with neither a shift nor a broadening of the intraband signal, see **Figure 2**a. It has been previously reported in HgSe NCs, also displaying intraband absorption[33], that such a transition indeed presents a weak temperature dependence. The temperature-induced shift was also observed to be weaker for less confined particles[33]. In this temperature range where the thermal energy k_BT is in the 5-25 meV range, the thermal activation of carriers remains high and no narrowing of the optical feature is observed.

Once capped with short ligands, here a mixture of mercaptoethanol and $HgCl_2$ ions[34,35], the I-V curves were measured over the 2-300 K range, see **Figure 2**b and S4. Above 20 K, I-V curves present an ohmic character. Below this value, the curves acquire a superlinear behavior, characteristic of transport in semiconductors at low temperature. The current as a function of temperature (inset of **Figure 2**b) follows an Arrhenius behavior over the whole temperature range. The associated activation energy is determined to be 1.5 meV. This value is consistent with the particle charging energy[36] (E_C) for these particles, which is given by the expression $E_C = \frac{e^2}{4\pi\varepsilon_0\varepsilon_r}\frac{s}{(R+s)R}$ =1.1 meV with ε_0 the vacuum permittivity, $\varepsilon_r = 15.2$ dielectric constant[37] of HgTe, R=7 nm the particle radius and s=1.5 nm the particle spacing.

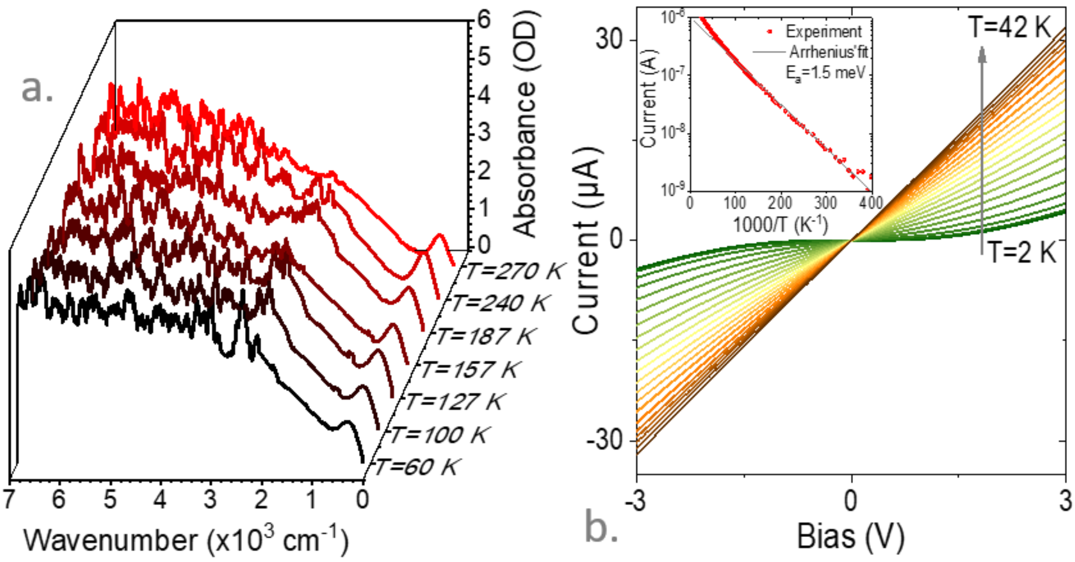

Figure 2 Impact of temperature*. a. Infrared spectra of THz HgTe NCs obtained at various temperatures. b. I-V curves from a thin film of THz HgTe NCs at various temperatures from 2 K to 42 K by steps of 2 K. Curves at higher temperatures are given in Figure S1. The inset shows the current as a function of temperature under constant drain source bias (V= 100 mV). A fit of the curve to the Arrhenius equation leading to a 1.5 meV activation energy is also provided.*

We then add a gate to the system to control the carrier density and determine the nature of the majority carriers. At room temperature, we use an electrolyte gating which enables low driving biases thanks to its large capacitance. In this case, the transfer curve appears as ambipolar with conduction under both negative (*i.e.* hole injection) and positive (*i.e.* electron injection) gate bias, see **Figure 3**a. There is nevertheless a clear prevalence for electron conduction. This is consistent with a degenerated electron doping through the observation of intraband absorption. Furthermore, we have performed thermoelectric measurements to determine the sign and magnitude of the Seebeck coefficient, which we found to be -83±3 µV.K^{-1}. This negative Seebeck coefficient further confirms the n-type nature of the material[35]. Secondly, for interband MWIR absorbing HgTe samples, we also observe a negative value of Seebeck coefficient (typically ≈ -301±9 µV.K^{-1}) proving that electron transport dominates conduction. However, a lower absolute value of Seebeck coefficient for the THz absorbing dots confirms that these are degenerately doped and demonstrate intraband absorption – thus validating the optical measurements.

At low temperatures, we switch to a more conventional dielectric gating based on SiO_2, since ion freezing occurring in electrolyte induces a loss of gate effect. Down to 10 K, the transport preserves its ambipolar character, see **Figure 3**b and c, though the current modulation gets weak. At very low temperatures, below 4 K, we observe that the transfer curve displays electron conduction only. This may result from a shift of the Fermi level deeper in the conduction band, but a freezing of the holes due to their large mass cannot be excluded.

Mobility values were extracted using the expression $\mu = \frac{L}{W\, C_\Sigma\, V_{ds}} \frac{\partial I_{ds}}{\partial V_{gs}}$, where L is the distance between the electrodes, W their length, and C_Σ the capacitance. The mobilities, as shown in **Figure 3**e, appear thermally activated. At 40 K, electron and hole mobilities reach 0.3 cm^2.V^{-1}.s^{-1} and drop down to 10^{-3} cm^2.V^{-1}.s^{-1} at 2 K.

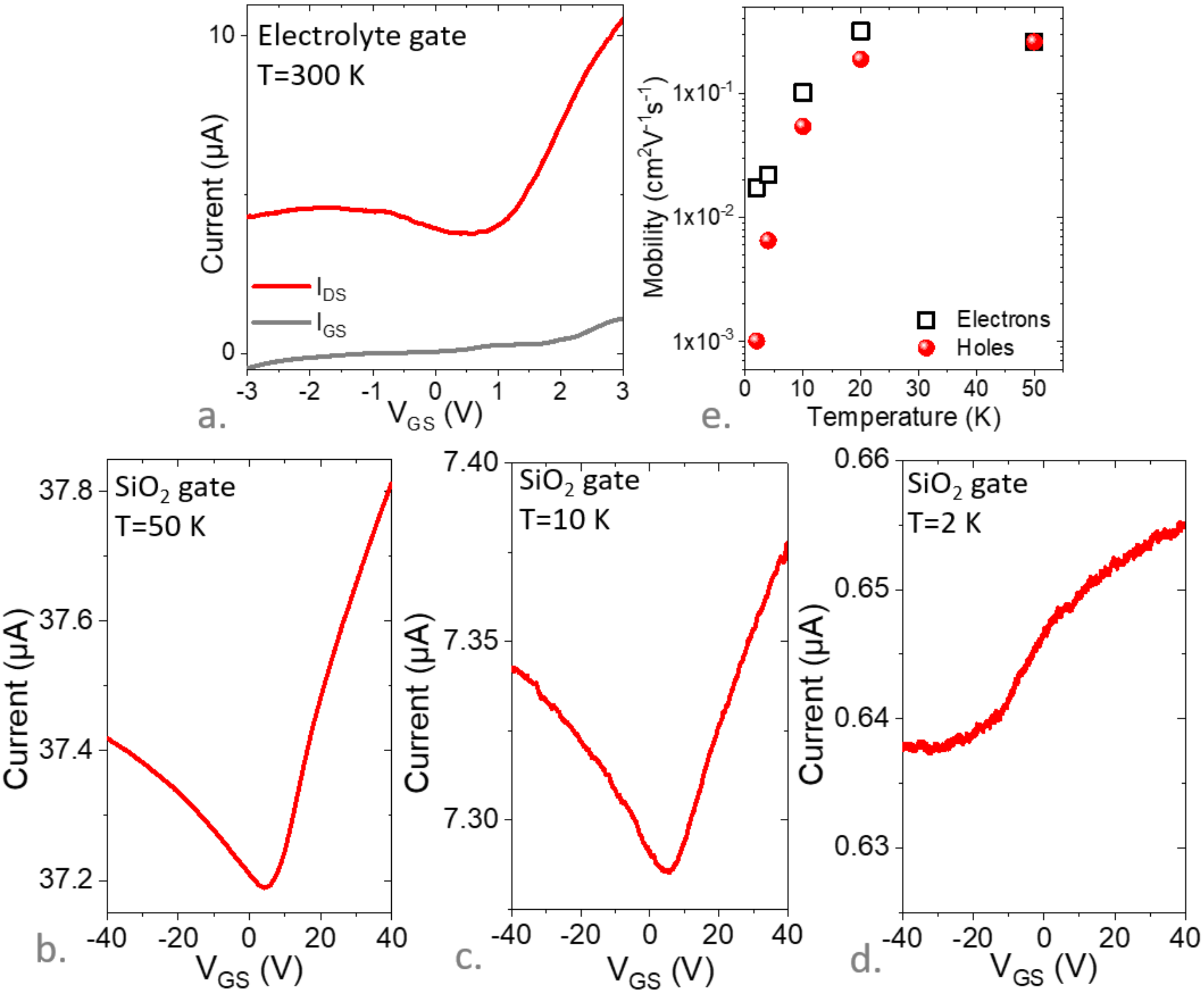

Figure 3 Transistor measurements. *a. Transfer curve (i.e. drain and gate current as a function of the applied gate bias under constant drain source bias-*V_{DS}*=0.05 V) for a THz HgTe NCs gated with an electrolyte at room temperature. Transfer curve (i.e. drain and gate current as a function of the applied gate bias under constant drain source bias-*V_{DS}*=1 V) for a THz HgTe NCs with a back silica*

substrate (t_{SiO2}=300 nm) at 50 K (b.), 10 K (c.) and 2 K (d.). e. Electron and hole mobilities as a function of temperature.

We then explored the impact of pressure and conducted a joint structural and spectroscopic investigation. HgTe under pressure is known to experience a series of structural phase transitions:[29–31] zinc blende to cinnabar (threshold pressure[31,38] $P_{ZB\rightarrow cinn} = 1.5 - 2.5\ \mathrm{GPa}$) and then to rock-salt above $P_{cinn\rightarrow RS} = 6 - 8\ \mathrm{GPa}$. These transitions occur at a fairly low pressure compared to what is observed in CdSe [39–42](transition from wurtzite to rock-salt occurs in the 3.6-5 GPa range) or PbS[43,44] NCs (no transition below 8 GPa). Such low pressure-induced phase changes might become a concern in the perspective of growing a core shell structure since the lattice mismatch between the core and the shell could generate a strain inducing an undesired phase change.

A series of X-ray diffraction patterns were acquired for pressures ranging from 0 to 12 GPa at room temperature, see **Erreur ! Source du renvoi introuvable.**a and S6, to monitor the structural phase change. The transition to the cinnabar phase is observed at about 2.9 GPa, as shown in detail in **Erreur ! Source du renvoi introuvable.**b. The peaks associated with the (111) and (200) planes (q=1.5 to 3 Å^{-1} range) of the zinc blende phase drastically reduce in amplitude as the pressure is increased, and the (102) peak of the cinnabar phase appears. There is clearly a range of pressures where both phases are present. The transition toward the rock salt is better illustrated in **Erreur ! Source du renvoi introuvable.**c, where the peaks related to the (110) and (201) planes of the cinnabar are transformed into a single peak attributed to the (220) plane of the rock-salt phase.

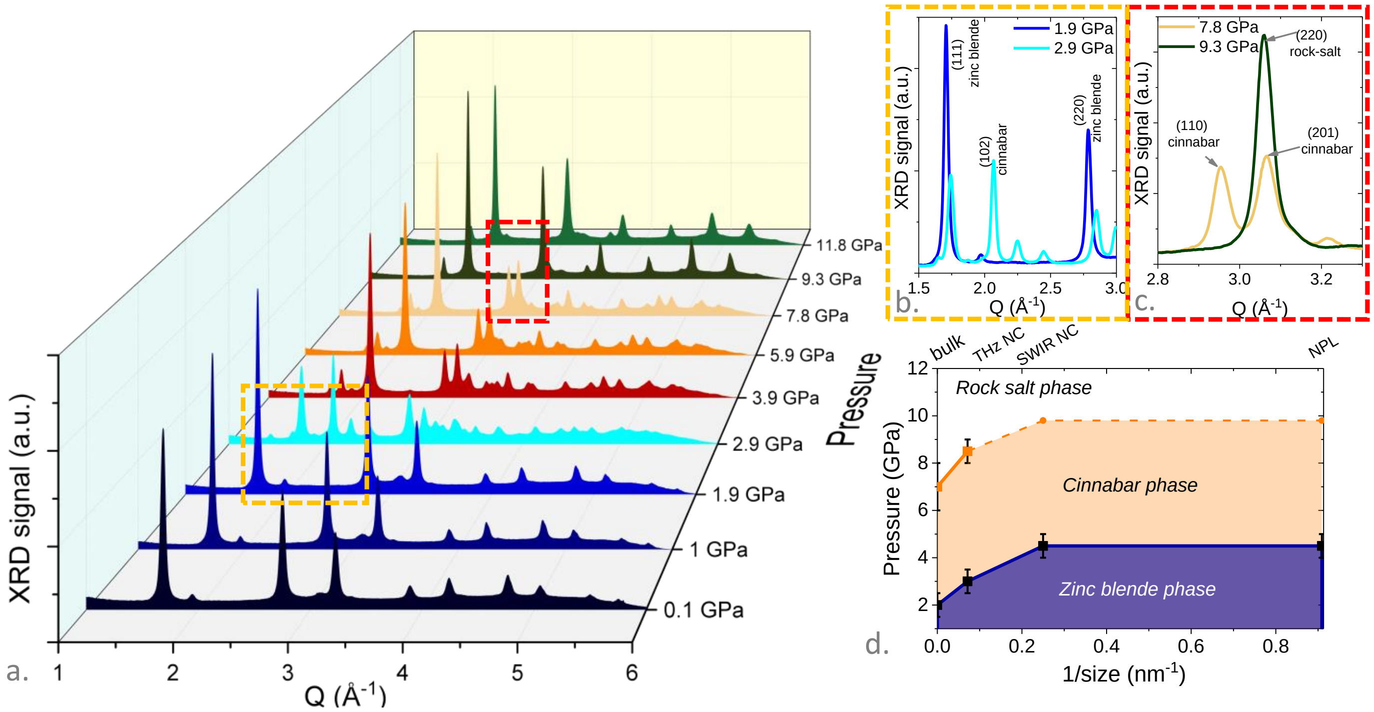

***Figure 4 Structural phase change in THz HgTe NCs probed by diffraction**. a. XRD pattern for THz HgTe NCs at room temperature and under various pressures. b. zoomed XRD pattern for two pressures around the transition from zinc blende to cinnabar. c. zoomed XRD pattern for two pressures around the transition from cinnabar to rock-salt. d. Threshold pressures for the zinc blende to cinnabar and cinnabar to rock-salt for various sizes of HgTe. Solid line is experimental data. Dashed line is extrapolated to match the dependence of the zinc blende to cinnabar transition. Values for bulk are taken from ref 38. Data from short wave infrared HgTe NCs are taken from ref 45. Data from HgTe nanoplatelets (NPLs) are taken from ref 28.*

As may have been anticipated[39–42], the threshold pressures are intermediate between the values observed for bulk[38] and the ones for strongly confined forms of HgTe NCs[28,45]. In **Erreur ! Source du renvoi introuvable.**d, we have proposed a phase diagram that shows how the finite size affects the existence diagram of each phase as a function of the particle size. In the case of CdSe, the pressure shift observed for smaller sizes has been attributed to additional surface energy as the particle size gets reduced[39–42].

As a result of the structural phase change, electronic phase changes have been observed[46] and predicted[31] in the bulk, but remains unexplored in the case of NCs. The zinc blende phase of HgTe is a semimetal (*i.e.* a gapless semiconductor) under bulk form, while the cinnabar and rock salt phase are respectively a semiconductor and a metal. We thus acquire a series of infrared spectra in the 0 to 10 GPa range, which corresponds to the range of existence of the three phases. To better observe the appearing and disappearing of a band gap, we use a broad band setup (7000-200 cm^{-1}) for which a schematic is proposed in Figure S7.

The zinc blende absorption spectrum (**Figure 1**b and **Figure 5**a) presents the intraband feature around 300 cm^{-1} and a long intense tail relative to the interband transitions in the mid infrared. In the zinc-blende phase, the pressure dependence of the interband absorption observed in **Figure 5** is qualitatively consistent with our previous modeling of HgTe nanocrystals and nanoplatelets under pressure using a multiband k.p formalism.[28] Quantitatively, as shown in the Figure S10, we observe roughly a 30 meV.GPa^{-1} blue shift of the interband absorption with pressure. Using the 14-band k.p modeling of reference 28, fitted to small HgTe nanocrystals and nanoplatelets, we predict a 32 meV/GPa at 60 K for the large nanocrystals. Considering the difficulty to pin-point precisely the interband absorption, the predicted energy shifts with pressure are in reasonable agreement with the spectroscopy, consolidating the set of pressure parameters that we use in the modeling.[28]

Above 2.5 GPa, the overall absorption signal collapses, see **Figure 5**a, and this results from the opening of a band gap in the bulk cinnabar phase[31]. Within this phase, we observe a clear redshift of the band gap with pressure (*i.e.* a band gap closing), also see **Figure 5**b. We found $\frac{dE_{cinn}}{dP}$=139 meV.GPa^{-1}, close to the value determined from transport measurements on the bulk[46] (159 meV.GPa^{-1}). This behavior is drastically different from the pressure dependence of the interband feature in the zinc blende phase for which an opening of the band gap was observed.[45] However, the latter effect was the result of the pressure on the quantum confinement though a modification of the effective mass of the electrons. Further exploration of this phase, in particular at even lower temperature, will be of utmost interest since the latter has been observed to be superconductive around 6 K.[47]

In the rock salt phase, the sample becomes strongly absorbent and the spectrum gets almost saturated over the whole spectral range. We attribute this behavior to the transition toward the metallic phase.

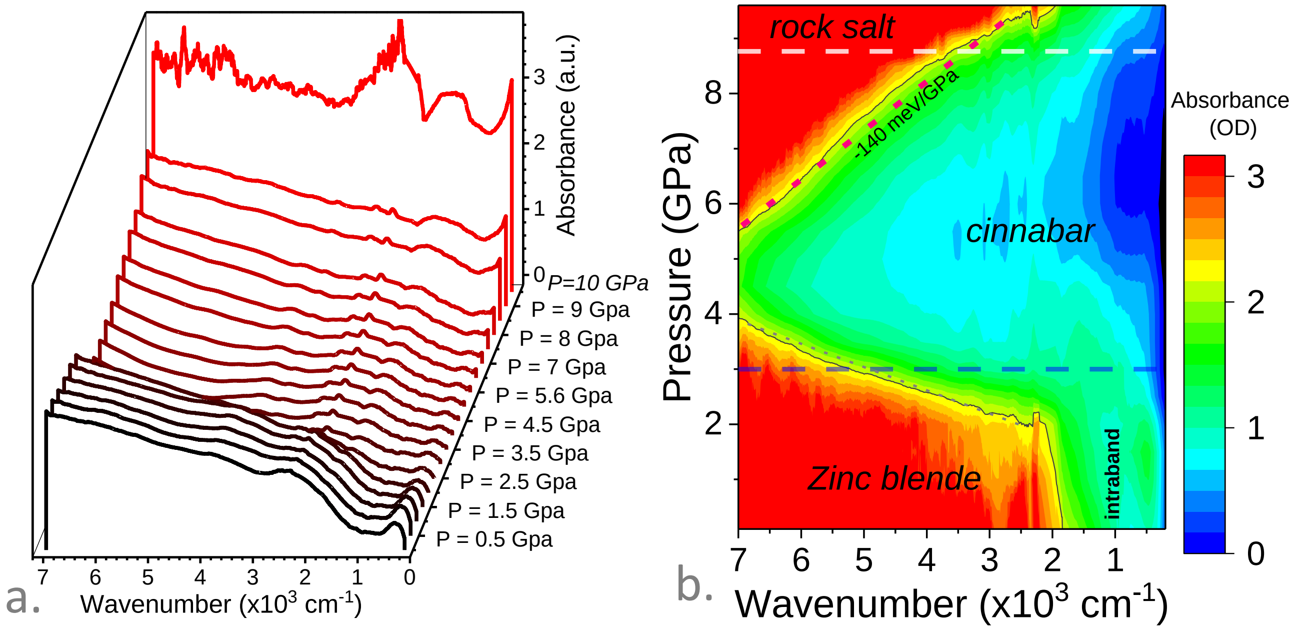

Figure 5 Electronic phase change in THz HgTe NCs probed by infrared spectroscopy under pressure. *a. Infrared spectra for THz HgTe NCs under various pressures, made at room temperature. Data obtained at 60 K are given in Figure S9. b. Infrared absorbance as a function of wavenumber and pressure for measurements conducted at 60 K. The thick dashed lines corresponds to threshold pressure for structural phase changes. The pink dotted lined shows the dependence of the band gap in the zinc blende and cinnabar phase.*

To conclude, we have explored the effect of temperature and pressure on the structural, spectroscopic and transport properties of 10 THz absorbing HgTe NCs. In the zinc blende phase, the particles display both interband and intraband absorption, which is consistent with the degenerate n-type nature also observed from transistor and thermoelectric measurements. The narrow band gap nature of the material enables both electron and hole conduction from room temperature down to 10 K and in this range the absorption spectrum is barely affected by the temperature (*i.e.* neither narrowing nor shift of the intraband feature). Only at very low temperatures (4 K and less) do we observe a change in behavior with the loss of hole conduction. Pressure impacts the structure and spectral properties in a far more dramatic way. Similarly to the bulk, HgTe NCs experience a series of phase changes from the zinc blende/semi-metallic phase toward the cinnabar/semiconductive and finally toward the rock salt/metallic phase. The domain of existence of the different phases appears shifted toward high pressure with respect to the bulk and we provide a phase diagram for these different phases as a function of the particle size.

Methods

Chemicals: Mercury chloride ($HgCl_2$, Sigma-Aldrich, 99%), **Mercury compounds are highly toxic. Handle them with special care.** Tellurium powder (Te, Sigma-Aldrich, 99.99%), silver nitrate (Alfa Aesar, 99.9 %), SnO_2 nanoparticles (15% dispersion in water, Alfa Aesar), trioctylphosphine (TOP, Alfa Aesar, 90%), oleylamine (OLA, Acros, 80-90%), dodecanethiol (DDT, Sigma-Aldrich, 98%), ammonium chloride (Alfa Aesar, 98 %) ethanol absolute (VWR), methanol (VWR, >98%), isopropanol (IPA, VWR), hexane (VWR, 99%), octane (Carlo erba, 99%), 2-mercaptoethanol (MPOH, Merck, >99%), N,N dimethylformamide (DMF, VWR), N-methylformamide (NMF, Alfa Aesar, 99%), toluene (VWR, 99.8 %). All chemicals are used without further purification except oleylamine that is centrifuged before use.

1 M TOP:Te precursor: 2.54 g of Te powder is mixed in 20 mL of TOP in a three neck flask. The flask is kept under vacuum at room temperature for 5 min and then the temperature is raised to 100 °C. Degassing of flask is conducted for the next 20 min. The atmosphere is switched to nitrogen and the temperature is raised to 275 °C. The solution is stirred until a clear orange coloration is obtained. The flask is cooled down to room temperature and the color changes to yellow. Finally, this solution is transferred to a nitrogen filled glove box for storage.

THz HgTe nanocrystal growth: 45 mL of oleylamine are introduced in a 100 mL three neck flask and then placed under vacuum and heated to 120 °C for 1 h. Then, the solution is placed under nitrogen atmosphere and heated to 200°C. A second solution is made by mixing 270 mg of $HgCl_2$ and 1 mL of TOP:Te (1 M) in 5 mL of oleylamine. The mercury and tellurium containing solution is quickly injected (within 2 min after mixing) in the hot oleylamine flask. The solution color immediately turns to dark brown, and the reaction is carried for 3 min. Then a mixture of 1 mL of dodecanethiol and 9 mL chloroform is injected slowly into the flask to quench the reaction. The content of the flask is split over two tubes and ethanol is added to precipitate the nanocrystals from the solution. The colorless supernatant is discarded and the formed pellet is redispersed in 3 mL of chlorobenzene. The NCs are washed again with ethanol and redispersed in 3 mL of chlorobenzene. This process is repeated a third time.

TEM For transmission electron microscopy (TEM) images, a drop of the NC solution is drop-casted onto a copper grid covered with an amorphous carbon film. The grid is degassed overnight to reduce future contamination. A JEOL 2010F is used for acquisition of images and operated at 200 kV.

Raman spectroscopy measurements were conducted at room temperature using a commercial confocal HORIBA LabRam HR Evolution micro-Raman microscope with a 100×objective and a 532 nm laser excitation. Spectra were recorded between 50 and 400 cm^{-1} with 1800 lines/mm grating resulting in a resolution of 1 cm^{-1}. Spectrometer calibration was set using the 520.5 cm^{-1} band of a Si crystal. The effective laser power at the exit of the objective was about 0.25 mW.

FTIR measurements at ambient pressure and room temperature were conducted in ATR configuration of an Thermo Fisher IS50 FTIR spectrometer to characterize the grown particles. The source is a globar, the beamsplitter is a Si wafer and the detector a DTGS. Acquisition was conducted with a 4 cm^{-1} resolution.

X-ray photoemission spectroscopy: The XPS measurements were conducted at the ANTARES beamline (SOLEIL synchrotron). A linear polarized light and a photon energy of 700 eV were used. The photoelectrons were collected with a new generation MBS A-1 analyzer. The overall energy resolution was better than 60 meV. All XPS measurements were performed at room temperature. The binding energy was calibrated using Au $4f_{7/2}$ photoemission peak which was set at 84.0 eV as an energy standard. For the deconvolution of the XPS spectra, a Shirley/linear background was subtracted and Voight function with 20% weighted Lorentzian contribution was used.

Electrode fabrication: Si/SiO_2 wafers are cut with an edge size of $1\ \mathrm{cm}$, cleaned by sonication in acetone and rinsed with acetone and isopropanol, then receive a 5 min oxygen plasma cleaning. An adhesion primer (TI-PRIME) is spin-coated on the substrate and baked at 120°C for 120 s. Then AZ5214E resist is spin-coated and baked at 110°C for 90 s. A MJB4 mask aligner is used to expose the substrates to UV light for 1.5 s through a lithography mask. Substrates are then baked at 125°C for 2 min to invert the resist and flood-exposed (i.e., without mask) for 40 s. Resist is developed using AZ726 developer for 32 s and rinsed with pure water. Patterned substrates are dried and cleaned with 5 min of oxygen plasma to remove resist residues. In a thermal evaporator, 5 nm of chromium are deposited as an adhesion promoter before 80 nm of gold are evaporated. Lift-off is conducted in an acetone bath.

Film deposition We dissolve 30 mg of $HgCl_2$ in a solution of 18 mL of DMF and 2 mL of mercaptoethanol. The original solution of HgTe nanoparticles is treated to obtain ligand exchange. At each step the solution is stirred with a vortex and sonicated. 1 mL of HgTe nanocrystals solution is mixed with 1 mL of the exchange solution. 5mL of hexane and 1 mL of DMF are added to the solution. The top phase is then removed, and the solution is washed three more times adding 5 mL of hexane and removing the top phase each time. Finally, the solution is centrifugated for 5 min at 6000 rpm to precipitate the nanoparticles. The supernatant is discarded, and the formed pellet is dried under primary vacuum for $1\ \mathrm{min}$ and then redispersed in 100 µL of DMF in order to target a thickness of about 150 nm. The obtained solution is called ink. Before ink deposition, the substrate is placed in an oxygen plasma cleaner for 2 min to promote adhesion. The ink is spin-coated on the substrate at 4000 rpm (at 2000 rpm.s^{-1} acceleration) for 5 min. This leads to a homogeneous deposition between 100 nm and 200 nm.

Electrolyte gating: For electrolyte gating we first mix in a glove box 0.5 g of $LiClO_4$ with 2.3 g of PEG (M_W = 10 kg.mol^{-1}). The vial is heated at 170°C on a hot plate for 2 h until the solution gets clear. To use the electrolyte, the solution is warmed around 100°C and brushed on the top of the HgTe film. The electrolyte is cooled to room temperature inside the glovebox, a copper grid is then applied on it to ease the electrical contact.

Transport measurements, *for measurements down to 15 K:* The sample is glued using a silver paste on a substrate of silicon covered with a gold layer and mounted on the cold finger of a cryostat. The gold layer is used as gate contact when transistor measurements are conducted. The transfer curves and the IV curves are measured using a Keithley 2634B sourcemeter; which applies biases and measures currents.

For measurements down to 2 K: A piece of alumina covered with a gold layer is glued on a sample holder using silver paste, and electrically connected using micro-soldering. The sample is glued using a silver paste on the gold layer and connected to the sample holder electrodes using silver paste. The gold layer is used as gate contact when transistor properties are studied. The transfer curves and the IV curves are measured using two Keithley 2400 as sourcemeters. The two instruments are used to drive the drain and gate respectively, while applying biases and measuring currents.

Thermoelectric measurements: Sheet resistance of each film was measured using Keithley 2400 Sourcemeters in 4-point van-der Pauw configuration. Film thickness was measured by scratching the film and measuring the step height with a Veeco Dektak 150 profilometer. Electrical conductivity of the bulk film was calculated by multiplying the sheet resistance with the thickness of each film. Seebeck coefficient (thermopower) was measured using a homemade probe setup where the thin film sample was placed across two Peltier devices. A constant current was passed through the two Peltier devices that were placed ≈4 mm apart, which heated up one side and cooled down the other, establishing a heat gradient across the sample. The temperature gradient (ΔT) was measured using two T-type thermocouples mounted in micromanipulators. The magnitude of the temperature gradient is directly correlated to the amount of current driven through the two Peltier devices. The induced open circuit voltage due to the ΔT was measured using Keithley 2000 multimeters. Normally, within one measurement, eight different thermal gradients were established, and 10 voltage measurements were recorded and averaged at each ΔT. For all samples, the open circuit voltage exhibited a linear relationship with ΔT. The Seebeck coefficient was calculated by obtaining the slope of the voltage vs. ΔT plot for each sample. Measurements were repeated and averaged. Electrical conductivity and Seebeck coefficient measurements were performed in a nitrogen-filled glovebox environment.

X-ray diffraction under pressure: Experiments were carried out using a membrane diamond anvil cell equipped with Boehler-Almax type anvils with 500 µm culets. A stainless-steel gasket of 200 µm thickness was pre-indented to 70 µm, provided with a 200 µm hole, and loaded with the sample, a 4:1 methanol-ethanol pressure transmitting medium and a 10 µm diameter ruby sphere which served as pressure marker. The "Mao hydrostatic" pressure scale was used to determine pressures. X-ray powder diffraction measurements were performed on a Rigaku MM007HF diffractometer equipped with a Mo rotating anode ($\lambda_{K\alpha 1}$ = 0.709319 Å, $\lambda_{K\alpha 2}$ = 0.713609 Å), Varimax focusing optics, and a RAXIS4++ image plate detector. X-ray data were collected at 20 °C. A LaB_6 standard sample was measured in the same experimental conditions to calibrate the Fit2D program, the image processing software used to integrate the intensities around the Debye-Scherrer rings and to get the 1D patterns.

Infrared spectroscopy under pressure: Membrane diamond anvil cells (DACs), equipped with IIas-type Boehler-Almax diamond avils with 600 µm culets, are used. Stainless steel gaskets with a thickness of 200 µm are indented down to 50 µm. A 250 µm hole is then drilled by electro-erosion. The gasket is placed on the top of one of the anvils, and the gasket hole filled with CsI, used a far infrared transparent pressure transmitting medium. After introducing a ruby crystal, the DAC is closed under gentle pressure until the salt forms a clear window. A drop of a diluted suspension of NCs in chlorobenzene is then added and dried on top of the CsI window to form a dry and uniform film of NCs. The DAC is then closed and introduced in a liquid He flow cryostat enabling high-pressure measurements at low temperature. The windows of the cryostat are made of polypropylene (PP) to optimize transmission in the far infrared, although some IR peaks of PP prevent measuring a few narrow spectral regions in the mid IR range. Then the cryostat is placed in a custom-made horizontal microscope available at the SMIS beamline of the synchrotron SOLEIL. The microscope is equipped with large working distance Schwartzschild objectives allowing to focus the incident infrared beam in the small optical aperture of the DAC inside the cryostat. The *in-situ* pressure is monitored by the ruby luminescence technique, where the signal is excited by a 532 nm laser and detected by an OceanOptics spectrometer, showing a characteristic doublet around 694 nm at ambient pressure. This photoluminescence is fitted and the pressure is computed using the R1 peak position. Once the pressure is stabilized, an infrared absorbance spectrum is acquired using a Thermo Fisher Nicolet iS50 FTIR with the synchrotron beam as source. To acquire a broad band spectrum, we use a KBr beamsplitter coupled to a MCT detector in the mid infrared (for the 7500-600 cm^{-1} range), while we use a silicon beamsplitter coupled with an InfraredLabs He cooled bolometer for detection (for the 700-150 cm^{-1} range). This operation is repeated for various pressures from 0 GPa to 10 GPa. When the maximum pressure is reached, the membrane is deflated and several spectra are acquired to check the reversibility of the pressure effect. The data processing procedure is described in figure S8.

ASSOCIATED CONTENT

Supporting Information include (*i*) material characterization, (*ii*) additional transport measurements at high temperature, (*iii*) X ray diffraction data and structural phase changes, (*iv*) description of infrared spectrum acquisition and data processing + infrared spectra at low temperature under pressure, and finally (*v*) k.p modeling of the pressure dependence of the band gap in the zinc blende phase.

COMPETING INTEREST

The authors declare no competing financial interest.

ACKNOWLEDGEMENTS

The project is supported by ERC starting grant blackQD (grant n° 756225). We acknowledge the use of clean-room facilities from the "Centrale de Proximité Paris-Centre". This work has been supported by the Region Ile-de-France in the framework of DIM Nano-K (grant dopQD). This work was supported by French state funds managed by the ANR within the Investissements d'Avenir programme under reference ANR-11-IDEX-0004-02, and more specifically within the framework of the Cluster of Excellence MATISSE and also by the grant IPER-Nano2 (ANR-18CE30-0023-01), Copin (ANR-19-CE24-0022), Frontal (ANR-19-CE09-0017), Graskop (ANR-19-CE09-0026) and NITQuantum (ANR-20-ASTR-0008-01), Bright (ANR-21-CE24-0012-02), MixDferro (ANR-21-CE09-0029) and Quickterra (ANR-22-CE09). Authors MS and AS acknowledge support by the US National Science Foundation (NSF) under Award ECCS-1809064 and the US Department of Defense (DOD) Office of Naval Research under Grant number N00014-20-1-2231 respectively.

REFERENCES

(1) Gréboval, C.; Chu, A.; Goubet, N.; Livache, C.; Ithurria, S.; Lhuillier, E. Mercury Chalcogenide Quantum Dots: Material Perspective for Device Integration. *Chem. Rev.* **2021**, *121*, 3627–3700.

(2) Kershaw, S. V.; Rogach, A. L. Infrared Emitting HgTe Quantum Dots and Their Waveguide and Optoelectronic Devices. *Z. Für Phys. Chem.* **2015**, *229*, 23–64.

(3) Geiregat, P.; Houtepen, A. J.; Sagar, L. K.; Infante, I.; Zapata, F.; Grigel, V.; Allan, G.; Delerue, C.; Van Thourhout, D.; Hens, Z. Continuous-Wave Infrared Optical Gain and Amplified Spontaneous Emission at Ultralow Threshold by Colloidal HgTe Quantum Dots. *Nat. Mater.* **2018**, *17*, 35–42.

(4) Qu, J.; Weis, M.; Izquierdo, E.; Mizrahi, S. G.; Chu, A.; Dabard, C.; Gréboval, C.; Bossavit, E.; Prado, Y.; Péronne, E.; *et al,* Electroluminescence from Nanocrystals above 2 µm. *Nat. Photonics* **2022**, *16*, 38–44.

(5) Shen, X.; Peterson, J. C.; Guyot-Sionnest, P. Mid-Infrared HgTe Colloidal Quantum Dot LEDs. *ACS Nano* **2022**, *16*, 7301-7308.

(6) Bossavit, E.; Qu, J.; Abadie, C.; Dabard, C.; Dang, T.; Izquierdo, E.; Khalili, A.; Gréboval, C.; Chu, A.; Pierini, S. *et al,* Optimized Infrared LED and Its Use in an All-HgTe Nanocrystal-Based Active Imaging Setup. *Adv. Opt. Mater.* **2022**, *10*, 2101755.

(7) Chen, M.; Lu, H.; Abdelazim, N. M.; Zhu, Y.; Wang, Z.; Ren, W.; Kershaw, S. V.; Rogach, A. L.; Zhao, N. Mercury Telluride Quantum Dot Based Phototransistor Enabling High-Sensitivity Room-Temperature Photodetection at 2000 nm. *ACS Nano* **2017**, *11*, 5614–5622.

(8) Gréboval, C.; Chu, A.; Magalhaes, D. V.; Ramade, J.; Qu, J.; Rastogi, P.; Khalili, A.; Chee, S.-S.; Aubin, H.; Vincent, G. *et al,* Ferroelectric Gating of Narrow Band-Gap Nanocrystal Arrays with Enhanced Light–Matter Coupling. *ACS Photonics* **2021**, *8*, 259–268.

(9) Gréboval, C.; Noumbe, U.; Goubet, N.; Livache, C.; Ramade, J.; Qu, J.; Chu, A.; Martinez, B.; Prado, Y.; Ithurria, S. *et al,* Field-Effect Transistor and Photo-Transistor of Narrow-Band-Gap Nanocrystal Arrays Using Ionic Glasses. *Nano Lett.* **2019**, *19*, 3981–3986.

(10) Noumbé, U. N.; Gréboval, C.; Livache, C.; Chu, A.; Majjad, H.; Parra López, L. E.; Mouafo, L. D. N.; Doudin, B.; Berciaud, S.; Chaste, *et al,* Reconfigurable 2D/0D p–n Graphene/HgTe Nanocrystal Heterostructure for Infrared Detection. *ACS Nano* **2020**, *14*, 4567–4576.

(11) Chu, A.; Gréboval, C.; Goubet, N.; Martinez, B.; Livache, C.; Qu, J.; Rastogi, P.; Bresciani, F. A.; Prado, Y.; Suffit, S. *et al,* Near Unity Absorption in Nanocrystal Based Short Wave Infrared Photodetectors Using Guided Mode Resonators. *ACS Photonics* **2019**, *6*, 2553–2561.

(12) Tang, X.; Ackerman, M. M.; Guyot-Sionnest, P. Thermal Imaging with Plasmon Resonance Enhanced HgTe Colloidal Quantum Dot Photovoltaic Devices. *ACS Nano* **2018**, *12*, 7362–7370.

(13) Zhu, B.; Chen, M.; Zhu, Q.; Zhou, G.; Abdelazim, N. M.; Zhou, W.; Kershaw, S. V.; Rogach, A. L.; Zhao, N.; Tsang, H. K. Integrated Plasmonic Infrared Photodetector Based on Colloidal HgTe Quantum Dots. *Adv. Mater. Technol.* **2019**, *4*, 1900354.

(14) Dang, T. H.; Abadie, C.; Khalili, A.; Gréboval, C.; Zhang, H.; Prado, Y.; Xu, X. Z.; Gacemi, D.; Descamps-Mandine, A.; Ithurria, S.; *et al,* Broadband Enhancement of Mid-Wave Infrared Absorption in a Multi-Resonant Nanocrystal-Based Device. *Adv. Opt. Mater.* **2022**, *10*, 2200297.

(15) Ciani, A. J.; Pimpinella, R. E.; Grein, C. H.; Guyot-Sionnest, P. Colloidal Quantum Dots for Low-Cost MWIR Imaging. In *Infrared Technology and Applications XLII*; SPIE, 2016; Vol. 9819, pp 333–341.

(16) Gréboval, C.; Darson, D.; Parahyba, V.; Alchaar, R.; Abadie, C.; Noguier, V.; Ferré, S.; Izquierdo, E.; Khalili, A.; Prado, *et al,* Photoconductive Focal Plane Array Based on HgTe Quantum Dots for Fast and Cost-Effective Short-Wave Infrared Imaging. *Nanoscale* **2022**, 14, 9359-9368

(17) Chu, A.; Martinez, B.; Ferré, S.; Noguier, V.; Gréboval, C.; Livache, C.; Qu, J.; Prado, Y.; Casaretto, N.; Goubet, N. *et al,* HgTe Nanocrystals for SWIR Detection and Their Integration up to the Focal Plane Array. *ACS Appl. Mater. Interfaces* **2019**, *11*, 33116–33123.

(18) Guzelturk, B.; Trigo, M.; Delaire, O.; Reis, D. A.; Lindenberg, A. M. Dynamically Tunable Terahertz Emission Enabled by Anomalous Optical Phonon Responses in Lead Telluride. *ACS Photonics* **2021**, *8*, 3633–3640.

(19) Goubet, N.; Jagtap, A.; Livache, C.; Martinez, B.; Portalès, H.; Xu, X. Z.; Lobo, R. P. S. M.; Dubertret, B.; Lhuillier, E. Terahertz HgTe Nanocrystals: Beyond Confinement. *J. Am. Chem. Soc.* **2018**, *140*, 5033–5036.

(20) Rinnerbauer, V.; Hingerl, K.; Kovalenko, M.; Heiss, W. Effect of Quantum Confinement on Higher Transitions in HgTe Nanocrystals. *Appl. Phys. Lett.* **2006**, *89*, 193114.

(21) Choi, D.; Yoon, B.; Kim, D.-K.; Baik, H.; Choi, J.-H.; Jeong, K. S. Major Electronic Transition Shift from Bandgap to Localized Surface Plasmon Resonance in $Cd_xHg_{1-X}Se$ Alloy Nanocrystals. *Chem. Mater.* **2017**, *29*, 8548–8554.

(22) Kim, J.; Choi, D.; Seob Jeong, K. Self-Doped Colloidal Semiconductor Nanocrystals with Intraband Transitions in Steady State. *Chem. Commun.* **2018**, *54*, 8435–8445.

(23) Jagtap, A.; Livache, C.; Martinez, B.; Qu, J.; Chu, A.; Gréboval, C.; Goubet, N.; Lhuillier, E. Emergence of Intraband Transitions in Colloidal Nanocrystals. *Opt. Mater. Express* **2018**, *8*, 1174–1183.

(24) Sahu, A.; Khare, A.; D. Deng, D.; J. Norris, D. Quantum Confinement in Silver Selenide Semiconductor Nanocrystals. *Chem. Commun.* **2012**, *48*, 5458–5460.

(25) Scimeca, M. R.; Mattu, N.; Paredes, I. J.; Tran, M. N.; Paul, S. J.; Aydil, E. S.; Sahu, A. Origin of Intraband Optical Transitions in Ag_2Se Colloidal Quantum Dots. *J. Phys. Chem. C* **2021**, *125*, 17556–17564.

(26) Apretna, T.; Massabeau, S.; Gréboval, C.; Goubet, N.; Tignon, J.; Dhillon, S.; Carosella, F.; Ferreira, R.; Lhuillier, E.; Mangeney, J. Few Picosecond Dynamics of Intraband Transitions in THz HgTe Nanocrystals. *Nanophotonics* **2021**, *10*, 2753–2763.

(27) Ruppert, M.; Bui, H.; Sagar, L. K.; Geiregat, P.; Hens, Z.; Bester, G.; Huse, N. Intraband Dynamics of Mid-Infrared HgTe Quantum Dots. *Nanoscale* **2022**, *14*, 4123–4130.

(28) Moghaddam, N.; Gréboval, C.; Qu, J.; Chu, A.; Rastogi, P.; Livache, C.; Khalili, A.; Xu, X. Z.; Baptiste, B.; Klotz, S. *et al,* The Strong Confinement Regime in HgTe Two-Dimensional Nanoplatelets. *J. Phys. Chem. C* **2020**, *124*, 23460–23468.

(29) Saini, pawan K.; Singh, D.; Ahlawat, D. S. Calculations of Electronic Band Structure and Optical Properties of HgTe under Pressure. *Indian J. Pure Appl. Phys. IJPAP* **2017**, *55*, 649–654.

(30) Chen, X.; Wang, Y.; Cui, T.; Ma, Y.; Zou, G.; Iitaka, T. HgTe: A Potential Thermoelectric Material in the Cinnabar Phase. *J. Chem. Phys.* **2008**, *128*, 194713.

(31) Duz, I.; Kart, H. H.; Kart, S. O.; Kuzucu, V. Theoretical Investigations on HgTe Chalcogenide Materials under High Pressure. *Phys. Scr.* **2021**, *96*, 045703.

(32) Krishtopenko, S. S.; Yahniuk, I.; But, D. B.; Gavrilenko, V. I.; Knap, W.; Teppe, F. Pressure- and Temperature-Driven Phase Transitions in HgTe Quantum Wells. *Phys. Rev. B* **2016**, *94*, 245402.

(33) Martinez, B.; Livache, C.; Notemgnou Mouafo, L. D.; Goubet, N.; Keuleyan, S.; Cruguel, H.; Ithurria, S.; Aubin, H.; Ouerghi, A.; Doudin, *et al,* HgSe Self-Doped Nanocrystals as a Platform

to Investigate the Effects of Vanishing Confinement. *ACS Appl. Mater. Interfaces* **2017**, *9*, 36173–36180.

(34) Martinez, B.; Ramade, J.; Livache, C.; Goubet, N.; Chu, A.; Gréboval, C.; Qu, J.; Watkins, W. L.; Becerra, L.; Dandeu, E. *et al,* HgTe Nanocrystal Inks for Extended Short-Wave Infrared Detection. *Adv. Opt. Mater.* **2019**, *7*, 1900348.

(35) Lan, X.; Chen, M.; Hudson, M. H.; Kamysbayev, V.; Wang, Y.; Guyot-Sionnest, P.; Talapin, D. V. Quantum Dot Solids Showing State-Resolved Band-like Transport. *Nat. Mater.* **2020**, *19*, 323–329.

(36) Zabet-Khosousi, A.; Dhirani, A.-A. Charge Transport in Nanoparticle Assemblies. *Chem. Rev.* **2008**, *108*, 4072–4124.

(37) Baars, J.; Sorger, F. Reststrahlen Spectra of HgTe and $Cd_xHg_{1-X}Te$. *Solid State Commun.* **1972**, *10*, 875–878.

(38) San-Miguel, A.; Wright, N. G.; McMahon, M. I.; Nelmes, R. J. Pressure Evolution of the Cinnabar Phase of HgTe. *Phys. Rev. B* **1995**, *51*, 8731–8736.

(39) Tolbert, S. H.; Alivisatos, A. P. Size Dependence of a First Order Solid-Solid Phase Transition: The Wurtzite to Rock Salt Transformation in CdSe Nanocrystals. *Science* **1994**, *265*, 373–376.

(40) Jacobs, K.; Wickham, J.; Alivisatos, A. P. Threshold Size for Ambient Metastability of Rocksalt CdSe Nanocrystals. *J. Phys. Chem. B* **2002**, *106*, 3759–3762.

(41) Jacobs, K.; Zaziski, D.; Scher, E. C.; Herhold, A. B.; Paul Alivisatos, A. Activation Volumes for Solid-Solid Transformations in Nanocrystals. *Science* **2001**, *293*, 1803–1806.

(42) Tolbert, S. H.; Alivisatos, A. P. The Wurtzite to Rock Salt Structural Transformation in CdSe Nanocrystals under High Pressure. *J. Chem. Phys.* **1995**, *102*, 4642–4656.

(43) Zhang, H.; Zhang, G.; Wang, J.; Wang, Q.; Zhu, H.; Liu, C. Structural and Electrical Transport Properties of PbS Quantum Dots under High Pressure. *J. Alloys Compd.* **2021**, *857*, 157482.

(44) Bian, K.; Richards, B. T.; Yang, H.; Bassett, W.; Wise, F. W.; Wang, Z.; Hanrath, T. Optical Properties of PbS Nanocrystal Quantum Dots at Ambient and Elevated Pressure. *Phys. Chem. Chem. Phys.* **2014**, *16*, 8515–8520.

(45) Livache, C.; Goubet, N.; Gréboval, C.; Martinez, B.; Ramade, J.; Qu, J.; Triboulin, A.; Cruguel, H.; Baptiste, B.; Klotz, S.; *et al,* Effect of Pressure on Interband and Intraband Transition of Mercury Chalcogenide Quantum Dots. *J. Phys. Chem. C* **2019**, *123*, 13122–13130.

(46) Ohtani, A.; Seike, T.; Motobayashi, M.; Onodera, A. The Electrical Properties of HgTe and HgSe under Very High Pressure. *J. Phys. Chem. Solids* **1982**, *43*, 627–632.

(47) Li, Q.; Zhang, J.; Zheng, Q.; Guo, W.; Cao, J.; Jin, M.; Zhang, X.; Li, N.; Wu, Y.; Ye, X. *et al,* Pressure-Induced Superconductivity in HgTe Single-Crystal Film. *Adv. Sci.* **2022***, 9,* 2200590.